POLITECNICO DI TORINO
Repository ISTITUZIONALE

Standardization of Cu2O nanocubes synthesis: Role of precipitation process parameters on physico-chemical and photo-electrocatalytic properties

Original
Standardization of Cu2O nanocubes synthesis: Role of precipitation process parameters on physico-chemical and photo-electrocatalytic properties / Cuatto, G., Zoli, M., Gallone, M., GUZMAN MEDINA, H.D.C., Castellino, M., Hernandez, S.. - In: CHEMICAL ENGINEERING RESEARCH & DESIGN. - ISSN 0263-8762. - 199:(2023), pp. 384-398. [10.1016/j.cherd.2023.09.047]

Availability:
This version is available at: 11583/2984205 since: 2024-06-12T14:19:56Z

Publisher:
Elsevier

Published
DOI:10.1016/j.cherd.2023.09.047

Terms of use:

This article is made available under terms and conditions as specified in the corresponding bibliographic description in the repository

Publisher copyright

(Article begins on next page)

01 November 2026

Available online at www.sciencedirect.com

Chemical Engineering Research and Design

journal homepage: www.elsevier.com/locate/cherd

Standardization of Cu_2O nanocubes synthesis: Role of precipitation process parameters on physico-chemical and photo-electrocatalytic properties

Giulia Cuatto, Maddalena Zoli, Mario Gallone, Hilmar Guzmán, Micaela Castellino, Simelys Hernández *

CREST group, Department of Applied Science and Technology (DISAT), Politecnico di Torino, C.so Duca degli Abruzzi, 24, 10129 Turin, Italy

ARTICLE INFO

Article history:
Received 12 July 2023
Received in revised form
27 September 2023
Accepted 29 September 2023
Available online 2 October 2023

Keywords:
Tuneable morphology
Cu_2O nanocubes
Synthesis standardization
Precipitation
Photoelectrochemical CO_2 conversion
Water reduction

ABSTRACT

A facile, reproducible, and scalable wet precipitation method was optimized to synthetise Cu_2O nanocubes with tuneable morphology and photocatalytic properties. The synthesis process was standardized by controlling the flow rate of addition of the reducing agent. This allowed to control the Cu_2O crystallites size, which decreased from 60 nm to 30 nm by increasing the L-ascorbic acid flow rate, while maintaining a high yield (ranging from 87% to 97%) and reproducibility, as confirmed by X-Ray diffraction, scanning electron microscopy, and X-Ray photoelectron spectroscopy analyses. Moreover, the role of the synthesis conditions on the Cu_2O nanocubes specific surface area and electrochemical surface area (ECSA) were investigated and correlated to their photo-electrocatalytic activity for the reduction of water and CO_2 under ambient conditions, on electrodes made by air brushing. Decreasing of the Cu_2O crystallites size enhanced the photo-electrocatalytic activity most probably due to a superior surface area, ECSA and an optimum valence and conduction band positions, which improves the charge transfer properties of the photocatalyst. The here proposed methodology and outcomes are very promising for the scale-up of the precipitation synthesis, not only of Cu_2O but also of other nanostructured metal oxides to be exploited as photo-catalysts for environmental and energy applications.

© 2023 The Author(s). Published by Elsevier Ltd on behalf of Institution of Chemical Engineers. This is an open access article under the CC BY-NC-ND license (http://creativecommons.org/licenses/by-nc-nd/4.0/).

1. Introduction

Since the industrial revolution, technological advancements and rapid population growth have led to a significant increase in energy demand, corresponding to a rise of anthropogenic CO_2 emissions, which has a big role in the continuous increasing of the atmospheric CO_2 concentration. (Blunden and Arndt, 2020) The problem is the relative velocity of its growth: from 1990 to 2019, the CO_2 concentration increased by 167%. In 2019, the emitted CO_2 was 38±3 $GtCO_2$-eq (data from IPCC Sixth Assessment report(Shukla et al., 2022)), equal to 64% of the greenhouse gases emitted globally that year. The CO_2 concentration in the air led from 280 ppm to 417.19 ppm (data updated to 5 September 2022, supplied from Mauna Loa Observatory, Hawaii(Biesbroek et al., 2022)). CO_2 emissions reduction is essential to pursue the global objectives of temperature increase containment defined in treaties such as the Paris Agreement (Unfccc, n.d.) and the Glasgow Conference Agreement ("Report of the Conference of the Parties on its twenty-sixth session, held in Glasgow from 31 October to 13 November, 2021," 2032). To this purpose, the development of renewable-energy-driven

* Corresponding author.
E-mail address: simelys.hernandez@polito.it (S. Hernández).

https://doi.org/10.1016/j.cherd.2023.09.047

0263-8762/© 2023 The Author(s). Published by Elsevier Ltd on behalf of Institution of Chemical Engineers. This is an open access article under the CC BY-NC-ND license (http://creativecommons.org/licenses/by-nc-nd/4.0/).

technologies, the use of green fuels (like green H_2), as well as the carbon capture, storage, and utilization, are promising solutions for controlling CO_2 emissions. CO_2 capture is an efficient way to decrease the quantity of carbon dioxide in the atmosphere, but CO_2 conversion and re-use is needed to close the carbon cycle loop.

CO_2 is a stable molecule from the thermodynamic point of view: it is the most oxidated state of carbon, with an oxidation number of + 4. The electron transfer is not energetically favourable since they should be forced to occupy the antibonding lowest unoccupied molecular orbital (LUMO) of the CO_2 molecule. It becomes necessary to develop catalysts able to lower the activation energy of this process. Direct routes for CO_2 reduction reaction (CO_2RR) may be carried out by thermal catalysis, electrocatalytic and photo-electrocatalytic processes (Das et al., 2020). Thermal catalysis takes advantage of more favourable kinetics, whereas electrochemical reduction could combine the two steps of generating hydrogen in situ from water splitting and CO_2 reduction via the hydrogenation route. On the other hand, photo-electrochemical reduction is based on semiconductor materials exploiting light to convert CO_2.

The photoelectrochemical reduction of water (to produce H_2) and of CO_2 (to generate added-value chemicals) is based on photocatalysts materials that can absorb light and act as a catalyst. Thermodynamically, the pure photo-reduction is favourable if the energy band gap is tuned to obtain a photo-excited electron with higher energy than the H_2O and CO_2 LUMO. The optimal energy band gap value for photoactivity is around 1.5 eV (a red component of the visible electromagnetic spectrum), but to obtain an optimal photocatalyst able to provide sufficient driving force for the reaction, an energy band gap of 2.0 eV (yellow/green component) is necessary (Osterloh, 2008). The development in nanomaterials synthesis provides opportunities to tune effective catalysts for specific reactions. Nanomaterials are also useful in optimizing the photoexcited electron lifetime: the shorter the distance between the photo-couple generation (electron-hole pair) and the surface, the lower the rate of possible recombination.

Among the semiconductor materials, cuprous oxide Cu_2O has an energy band structure suitable for both the water reduction to H_2 and the CO_2 reduction to CO and C_{1+} molecules (containing one carbon atom). The standard reduction potentials (E^0) for the H_2 evolution reaction (HER) and the CO_2 reduction reaction (CO_2RR) to CO are close to each other (0.00 V vs. RHE and –0.10 V vs. RHE, respectively), thus it is difficult to be selective towards one of them. Cu_2O is a very interesting transition metal oxides because of its low cost, non-toxicity and abundance (Sun et al., 2018). It is an intrinsic p-type semiconductor, acting as a photocathode because the Fermi energy level (E_F) is lower than the E^0 of the HER and CO_2RR to CO in aqueous electrolytes, so that the electrons can be transferred from the reagent in the electrolyte to the catalyst surface. The energy bands bend because an electric field is formed at the interface. It is also a very good photocatalyst reaching quantum efficiencies of up to 90% in some heterostructures (see Section S0 in the Supporting Information, SI). Cu_2O can be synthesized with several morphologies: normally, high index planes show high photo-activity, while the cubic morphology with low index facets has a higher selectivity for the CO_2RR against the HER (Handoko and Tang, 2013). A facile, cheap, scalable process for synthesising this catalyst is challenging. In this regards, previous works have documented the effectiveness of Cu-based catalysts towards CO_2RR (Ahmad et al., 2022; Woldu et al., 2022; Xie et al., 2018). Herein, the catalysts were prepared by wet precipitation (Zhang et al., 2019), but the synthesis conditions were tuned to obtain different physicochemical properties. In previous literature, only few works analysed the effect of the synthesis conditions on the obtained photocatalyst material. Likewise, the wet precipitation synthesis carried on this work was standardized by controlling the flow rate of the reagents to obtain reproducible characteristics of the Cu_2O nanocubes. The synthesis process conditions were correlated to the composition, morphology, surface area, UV-Vis light response and photoactivity of the catalyst. The samples reproducibility was assessed through X-Ray diffraction, X-Ray photoelectron spectroscopy, scanning electron microscopy, and direct reflectance UV–vis spectroscopy analyses. Some characteristics turn out to be tuneable by modifying the reagents flow rate. The crystallite size shows a strong dependence on reducing agent flow rate: higher the flow rate smaller the crystallite size. Therefore, properties like specific surface area and electrochemical surface area also changed with the flow rate, being inversely proportional to the crystallite sizes. Likewise, the Cu_2O photocatalytic properties were tuned by modifying the synthesis conditions: the maximum photocurrent density was obtained with the smaller crystallites of the Cu_2O nanocubes. Finally, to address the issue related to the Cu_2O degradation during the photo-electrochemical process a Cu_2O/SnO_2 heterostructure was studied. Over the past decade, significant works have been analysed the design and preparation of semiconductor heterostructures for both improving the photoconversion efficiency and steering the charge carriers. There are several types of heterojuntions: metal-semiconductor, semiconductor-semiconductor, graphene-semiconductor, and Z-scheme semiconductor heterostructures. The semiconductor-semiconductor heterostrustures get inspired from electronics. By varying the energy band gap of the two semiconductors and their alignment it is possible to obtain three different heterostructures: type I or straddling gap, type II or staggered gap, and type three or broken gap. The staggered gap heterostructure is very useful when it is needed a charge carrier spatial separation, like photocatalysis (Fang et al., 2020). By using heterostructures as catalysts it is possible to maximize carrier utilization efficiency. The addition or modification of the chemical composition, in terms of dopants, heterostructues, alloys, and defects may be an effective approach to activity enhancement. The characteristic size of the components, especially when it becomes nanometric, can likewise modify the charge dynamics (Tsao et al., 2021). The performances of the bare catalysts can be improved by exploting heterojunctions. By having a higher band gap the tin oxide layer can reduce energy losses and make the most of the solar spectrum. (Chiu et al., 2019). Severe photocorrosion is commonly observed when elements as Cu, S or Se are present in the catalyst. Some studies proposed many surface protection methods (Hsieh et al., 2020). Thus, a SnO_2 layer was chosen as a protective shell for the Cu_2O. The Cu_2O/SnO_2 core-shell material was prepared and tested, demonstrating the potential of such approach for stabilizing the photocatalyst activity and selectivity during the CO_2 photo-electrochemical reduction to syngas (a mixture of CO and H_2).

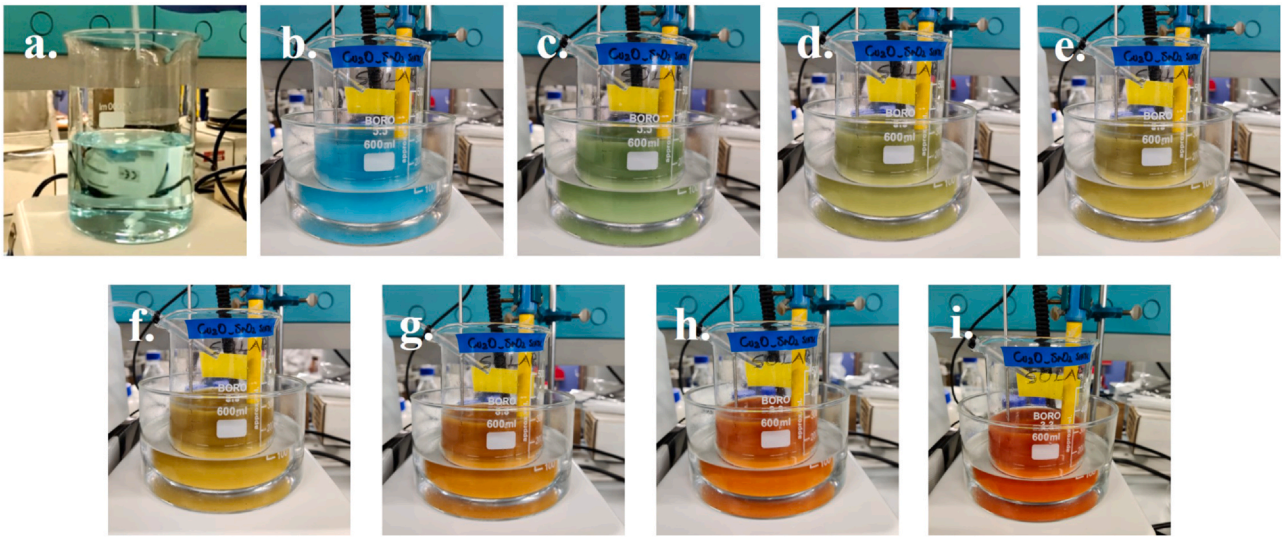


Fig. 1 – Colour changes during the synthesis process from light blue (a.) to opaque light blue due to the precipitation of Cu $(OH)_2$ (b.) and then to green, yellow, and orange after the addition of L-ascorbic acid and the formation of Cu_2O (from c. to i.).

2. Materials and methods

2.1. Materials

Cu_2O nanocubes were obtained using Copper Chloride $CuCl_2$ (99%) as copper oxide precursor, sodium hydroxide NaOH (≥98%) as a precipitant agent for copper hydroxide, and L-ascorbic acid $C_6H_8O_6$ as a reducing agent. All these reagents were purchased from Sigma Aldrich®. Each stage is conducted at room temperature with magnetic stirring on a thermal magnetic plate (provided by ARGO LAB) equipped with a thermocouple in a silicone oil bath (Sigma Aldrich). Ultrapure type 1 water (MilliQ) was used to prepare all the aqueous solutions and to clean glassware and instruments.

For the photoelectrochemical tests are needed Nafion (5% wt. il lower aliphatic alcohols and water, 15–20% water) and Ethanol (≥ 99.8%) for the ink manufacturing. $KHCO_3$ (99.7%) and KOH (ACS reagent, ≥85%, pellets) were used as electrolytes in the test cell.

2.2. Cu_2O synthesis

Cu_2O nanocubes were synthesized by wet precipitation, optimizing a procedure analogous to the one described in literature by Zhang et al.,(Zhang et al., 2019) but controlling the flow rates of the precursors during their mixing. Thus, 25 mL of NaOH aqueous solution 6 M was added to 250 mL of $CuCl_2$ aqueous solution 0.02 M. NaOH was added by exploiting a peristaltic pump (Gilson®) with a fixed velocity of 25 mL min^{-1}. The solution changes from light blue to intense blue as the $Cu(OH)_2$ particles precipitate. After 30 min, the L-ascorbic acid solution (the reducing agent) was added at different controlled flow rates, from 5 to 200 mL min^{-1}. Two peristaltic pumps were employed to reach the mentioned flow rates (purchased from Ismatec® and Liquiport®). That step caused an additional solution colour change from intense blue to green, then mustard yellow, until the suspension of Cu_2O stabilized at orange (Fig. 1). The pH value was monitored during the synthesis (pH meter, Milwaukee) at the four different process steps: i) $CuCl_2$ aqueous solution 0.02 M, ii) NaOH 6 M addition, iii) L-ascorbic acid 1.8 M introduction, and iv) after 3 h under stirring. The initial pH value is around 4, while after the NaOH solution addition it becomes alkaline and remains higher than 7 also after the L-ascorbic acid addition.

Afterwards, the suspension was left under stirring for three hours at 25 °C before vacuum filtration and MilliQ washing. A vacuum pump (provided by Steroglass) and cellulose nitrate membrane filter with a pore diameter of 0.2 µm (Whatman™) were used to filter the suspension. The filtered Cu_2O powder was subsequently dried in a vacuum oven (Büchi Labortechnik AG) at 60 °C overnight. The samples were named Cu_2O, followed by the L-ascorbic acid flow rate in mL min^{-1}. A progressive number was added at the end of name for samples with the same flow rate.

2.3. Physical characterization

X-Ray Diffraction (XRD) technique was carried out by using a diffractometer (Panalytical X'Pert PRO) working in Bragg-Brentano configuration and equipped with Cu Ka radiation (l =1.5418 Å) set at 40 kV and 40 mA. The spectra were used to evaluate the crystalline phases of the materials and the dimensions of the crystallites by using the Scherrer equation:

$crystallite\ size\,(Å) = k\lambda\,(Å)/FWHM\cos\theta$, where k is the shape factor (equal to 0.94), λ is the X-Ray wavelength (1.5418 Å), *FWHM* is the full width at half maximum of the diffraction peak and θ is the diffraction angle of the analyzed peak. The powder samples were examined in the 2θ range of 20–90° with a scanning step of 0.026°.

The energy band gap of the material was calculated via Diffuse Reflectance UV–vis spectroscopy (DR-UV–vis). Cu_2O is a semiconductor with an allowed direct band gap. The continuous data was plotted as the Kubelka-Munk function F(R) versus the wavelength λ (nm). From these results absorbance coefficient α versus energy in eV was calculated. Following the Tauc plot method (Feng et al., 2015; Haryński et al., 2022; Jubu et al., 2020; Sahoo et al., 2020), the absorbance is exponentiated at 1/r, where r is ½ for material with a direct (allowed) band gap. The curve α^2 versus energy exhibits a linear portion that corresponds to the material absorption. The Energy Band Gap (E_G) was extrapolated by the corresponding intersection between the linear fitting and abscissa axis.

The specific surface area evaluated according to the Brunauer–Emmett–Teller (BET) theory and the total pore volume were determined by measuring N_2 adsorption/desorption isotherms at 77 K in a volumetric equipment TriStar II 3020 (Micromeritics). All the samples were outgassed at 100 °C for 2 h before the measurements.

Field Emission Scanning Electron microscopy (FESEM) (ZEISS MERLIN), with an Energy Dispersive X-ray Spectroscopy System (EDS), conducted at 3 kV, was employed to obtain the morphology and the content of the relative elements of the samples. These amounts must be taken as semi-quantitative ones, as the technique is not able to do a quantitative evaluation of the elements without any reference. The samples were prepared by depositing a small amount of the particles on a conductive tape.

The ECSA was measured in a traditional three-electrodes cell configuration (see section S1 and Fig. S1 in SI). The prepared catalyst was deposited on the glassy carbon and used as the working electrode (WE, geometric area of 0.19625 cm^2). The catalytic ink consists of an ultrasonic dispersion of different components: i) the synthesized particles, ii) a Nafion solution as the binder (solution at 5%wt in water and 1-propanol from Sigma Aldrich), and ethanol (99% purity Sigma-Aldrich) used as a carrier for well dispersing all the components. The ink had a catalyst/Nafion ratio of 70/30 and a solid phase percentage of 3%. The dispersion was sonicated for 15 min before the drop-casting process. A volume of the catalytic ink was deposited onto the glassy carbon electrode to have the working electrode loading near 1 mg cm^{-2}. The electrode was dried with a slow rotation in air.

X-Ray Photoelectron Spectroscopy (XPS) measurements were performed by using a PHI 5000 Versa Probe (Physical Electronics) system with a monochromatic X-ray source of 1486.6 eV (Al K-alpha) to determine the surface composition of the prepared novel catalysts. The samples were prepared by attaching a thin layer of powder on a conductive tape to avoid surface powder charging. All core-level peak energies were referenced to C1s peak at 284.8 eV.

2.4. *Preparation of the electrodes*

The electrodes consisted of a thin film of Cu_2O over carbon paper (Toray™ carbon paper, thickness 0,19 mm Teflon™ 20 (+/– 5) wt% treated, Quintech). The catalyst ink was prepared as indicated in Section 2.3. It was deposited via nitrogen airbrushing technique on a batch of 4 electrodes, each masked with Teflon to make available 1 cm^2 as the deposition area. The electrodes were placed over a heating plate at 50 °C to reach a complete solvent evaporation. The tests were performed with a catalyst loading of 1 mg cm^{-2}.

2.5. *Photo-electrocatalytic CO_2 reduction tests*

The photo-electrochemical CO_2 reduction tests involve the catalytic activity evaluation in a three-electrodes H-type quartz reactor setup, as displayed in Fig. 2 (Qin et al., 2013; Wang et al., 2019) A $KHCO_3$ 0.1 M solution, under N_2 or CO_2 flow, was employed as the catholyte and a KOH 0.1 M solution was used as the anolyte. The cathodic and the anodic compartments were separated by a bipolar membrane (Fumatech), which was previously activated with H_2SO_4 0.1 M solution in the cathodic chamber and KOH 0.1 M in the anodic one. The three-electrode system included: a platinum mesh as the CE, an Ag/AgCl (3 M NaCl) electrode as the RE, and the Cu_2O-based prepared electrodes used as the WE. A Biologic VSP-300 multichannel potentiostat was used to carry out the electrochemical tests. The H-type cell is illuminated from the cathode side from the simulated AM 1.5 G solar light provided by using a 450 W Xe lamp by Newport equipped with an AM 1.5 filter and a water filter model 6123NS, with a power density of 1000 mW·cm^{-2}.

Before starting the experiments, the gas was bubbled into the solution for at least 20 min to saturate the electrolyte. First, the tests were conducted in N_2 to assess the behaviour of the system during the water reduction reaction. Then, the same measurements were conducted under a continuous CO_2 flow. Cyclic Voltammetry (CV) was performed from 0 V to –1.5 V vs. Ag/AgCl with a scan rate of 30 mV s^{-1} in the dark and light mode (three scans per mode) to evaluate the photoelectrochemical behaviour of the catalyst. Linear Sweep Voltammetry (LSV) from 0 V to –1.5 V vs. Ag/AgCl with a scan rate of 10 mV s^{-1} in chopped light mode (2 s) was carried out to evaluate the onset potential and the light influence. Chronoamperometry (CA) under CO_2 flow, in chopped light mode (60 s) for 10 min at different potential values, was followed up to evaluate the photocurrent gain, calculated as the current difference between the values obtained in light and dark modes. Additionally, chronopotentiometry (CP) was performed under CO_2 flow at –3 mA cm^{-2} for 2 h to estimate the stability of the catalyst and the product distribution of the reaction. During that test, the gases products were analysed with an online gas chromatograph (Varian 490-microGC) equipped with two channels, including a 10 m Rt-Molsieve 5 A column and an 8 m Rt-Q-Bond column, respectively, and thermal conductivity detectors (TCDs). The composition of the liquid products was analysed by using High-Performance Liquid Chromatography (HPLC) (Shimadzu) furnished with two detectors: RID-10A and PDA 212 nm. The column is a Rezex ROA Organic acid 300 × 7.8 mm with 5 mM H_2SO_4 aqueous solution as mobile phase. Moreover, the liquid samples were also characterized by using a Gas Chromatograph (Perkin Elmer GC, Clarus 580) equipped with a Head Space (Turbomatrix 16), a Stabilwax-DA column, and a Mass Spectrometer Detector (MSD, SQ8 S). Electrochemical Impedance Spectroscopy (EIS) in N_2 and CO_2 atmosphere, at potential equal to the onset (retrieved by the LSV curve) and the potentials used during the CA tests, were executed to compare the catalyst resistance to electron transfer on the electrode/electrolyte interphase. The plots obtained were fitted with the free-software EIS Spectrum Analyser (ABC Chemistry).

3. Results

3.1. *Physical-chemical characterization*

The copper oxide samples synthesized with the wet precipitation method were characterized to evaluate the effect of the L-ascorbic acid flow rate. Fig. 3a shows the XRD patterns of the synthesized Cu_2O powders. The defined reflections of all the samples were assigned to Cu_2O (reference pattern JCPDS 01–077–0199) with similar ratios between the peak intensities. However, CuO (reference pattern JDPS 01–080–0076) diffraction peaks were also detected in the samples Cu_2O_20_1 and Cu_2O_60_1. Fig. 3b compared the spectra of the samples synthesized with the same flow rate: 200 mL min^{-1}, demonstrating the replicability of the crystallites composition corresponding to the Cu_2O phase (the

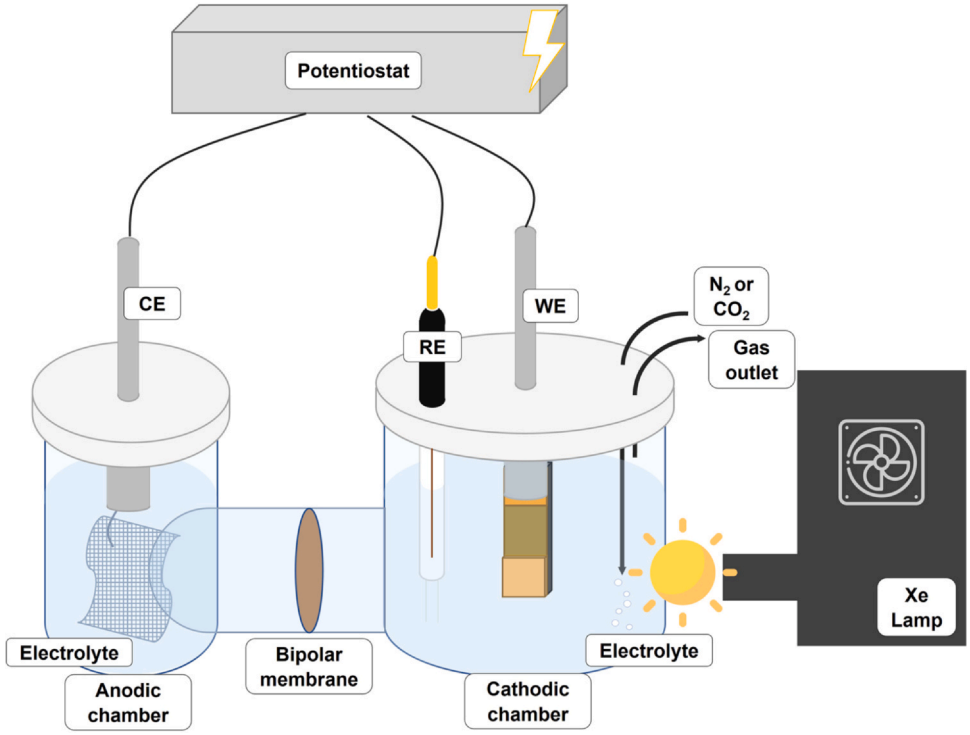


Fig. 2 – Two-chamber cell (H-cell) setup with three electrodes system (platinum mesh counter electrode CE, Ag/AgCl (3 M NaCl) reference electrode RE, and Cu_2O on carbon paper working electrode WE). Cathodic chamber illuminated with simulated AM 1.5 G solar light (Xe lamp). The gas inlet provides nitrogen or carbon dioxide to saturate the environment. The gas outlet carries gas products to the GC analyser.

spectra of Cu_2O_100 are reported as another example in Section S2, Fig. S2 in the SI). In particular, the most intense peaks are the same in both spectra, corresponding to the Cu_2O crystalline planes: (111), (200), and (220) at about 36.5°, 42.5°, and 52.6°, respectively (see Fig. 3b). The intensity ratio between the peaks (111) and (200) was analysed for all the prepared catalysts (see Fig. 3c). The mean value of such ratio is 3.19 ± 0.06, and a slight trend can be observed depending on the ascorbic acid flow rate. Nevertheless, considering the standard deviation of the values, the differences can be considered as negligible because they are all included in the deviation. Conclusively, no significant dependencies of the crystal growth directions on the L-ascorbic acid flow rate exist. For each sample the yield was calculated, resulting to be between 87% (for the lower velocity) and 97% (for the highest one).

The crystallites size of the Cu_2O phase on each sample was calculated from the Debye-Scherrer equation. The evaluated value is an average of the size of the crystalline domains corresponding to the (111), (200), and (220) planes. Fig. 4a shows the average crystallite sizes versus the L-ascorbic acid (reducing agent) flow rate. The prepared nanocatalysts are constituted by crystals lower than 100 nm. Interestingly, the crystallite size shows an appreciable dependency on the L-ascorbic acid flow rate. The higher the reagent flow rate, the lower the crystallites size. The samples synthesized with a flow rate equal to 100 mL min^{-1} present a value out of the trend, showing a high standard deviation. Fig. 5 demonstrates that by controlling the reducing agent flow rate it is possible to manage the crystal sizes of the samples.

The reproducibility of the synthesis was demonstrated, as shown in Fig. 4b and c. Fig. 4b and Fig. 4c displays the FESEM images of sample Cu_2O_200, showing the face-raised cubic morphology of the crystals (Huang et al., 2012). The FESEM micrographs of the remaining samples are provided in Section S3 in the SI.

The results of EDX analysis are reported in Table 1. Only Cu and O were detected, with a mean Cu:O ratio equals to 2. For the samples synthesized at a lower L-ascorbic acid flow rate, the ratio is slightly higher than two, while for the other samples, the values are somewhat lower. The analysis depth is around 1 µm, with an electron acceleration of 15 kV, thus the measure can be considered as affected by the surface where the copper can undergo oxidation. The DR-UV–vis analysis was performed to obtain the diffuse reflectance curve depending on the wavelength λ (nm). By using the Kubelka-Munk function, the diffuse reflectance was converted into absorbance $\alpha = [F(R)\cdot h\nu]^2$ versus energy in eV. At the beginning of the adsorption range, the curve increases with a linear trend. A linear fit was done in this region using the Origin PRO 2018 software. By taking the coefficients of the linear fitting, the intersection with the abscissa axis was calculated to obtain the energy gap. From the same coefficients, the error related to the measure was quantified. For all the samples, the percentual error is around 2%. Considering the error, the energy gap values are very similar, and the average value is equal to 2.49 ± 0.02 eV. The values are reported in Table 1: it is it is possible to attest the repeatability of the syntheses. This value is coherent with the literature: 2.50 eV for Cu_2O cubic nanoparticles bigger than 86 nm ("Semiconductor nanocrystals possessing broadly size- and facet-dependent optical properties | Enhanced Reader," n.d.).

The specific surface area was evaluated starting from the adsorption and desorption curves of nitrogen at 77 K and following the BET theory. The Cu_2O nanoparticles did not show any sign of a porous surface, as seen from the

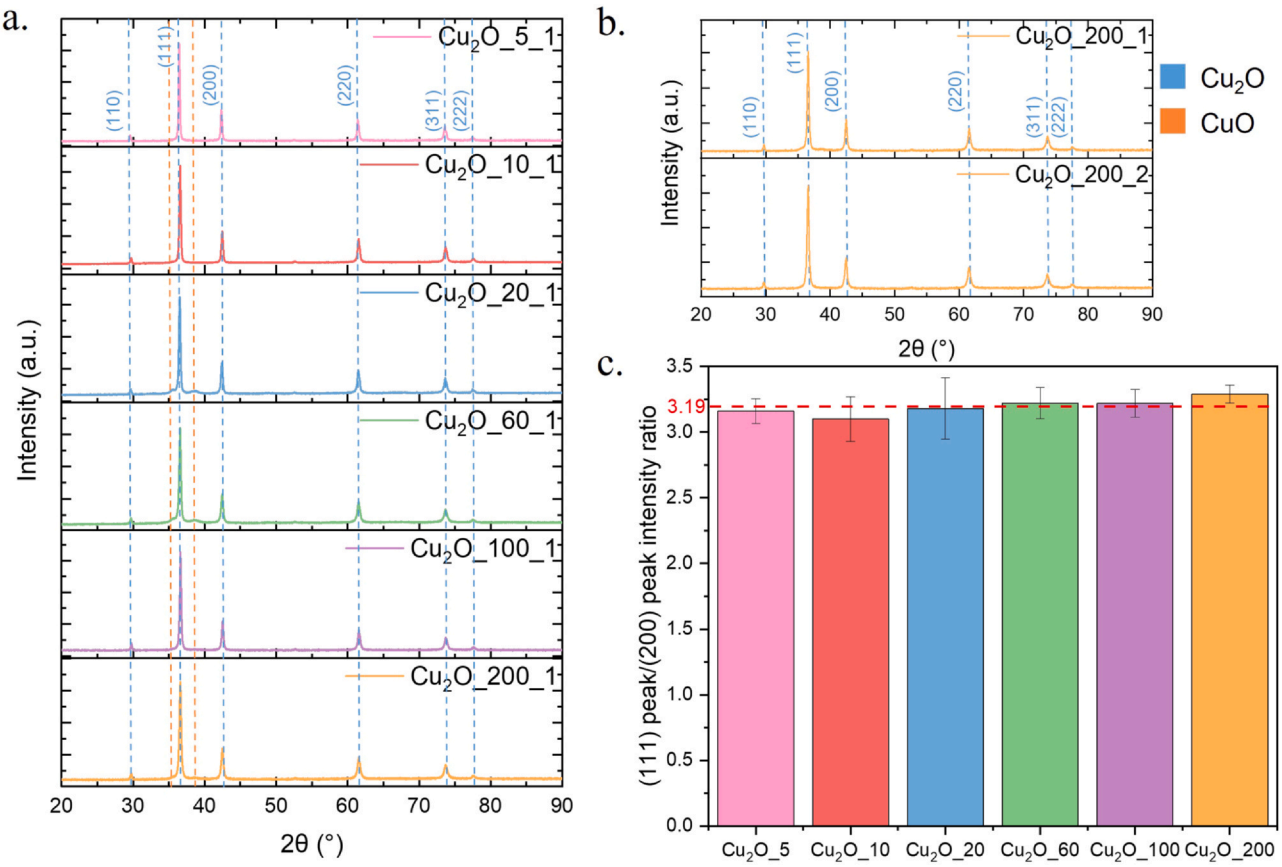


Fig. 3 – X-Ray Diffraction analysis: a. Spectra of one sample per group, b. Spectra of different samples synthesized under the same conditions, c. Average of peaks intensity ratio for each synthesis conditions group.

FESEM analysis. As expected, the BET curves do not have any relevant hysteresis (adsorption and desorption curves in Section S4, Fig. S5 in the SI). The specific surface area was obtained from the first linear portion of the adsorption curves. The values (reported in Table 1) are very small (lower than 10 $m^2\ g^{-1}$). For the Cu_2O_10 the value was equal to 0.51 ± 0.05, but it is too low, thus, it cannot be taken as reliable. However, it is clearly visible a general trend depending on the L-ascorbic acid flow rate. As expected, higher the flow rate higher the specific surface area. Nonetheless, the sample synthesized at 100 mL min^{-1} of L-ascorbic acid flow rate presents a lower value of specific surface area. This sample shows ahead an average crystallite size value non-coherent with the crystallite size trend (see Fig. 5). In terms of crystallite size the samples Cu_2O_100 present a higher value than the one expected, and a standard deviation bigger than the values obtained for the other samples. These bigger crystallites may led to the lower pore volume detected, and so to the lower specific surface area value.

The ECSA measurement shows a similar trend, with a value that starts from 0.99 cm^2 for Cu_2O_20 and shoots up to 2.42 cm^2 for the Cu_2O_60 sample (Fig. 5). The specific surface area and the electrochemical surface area were compared to the crystallites size since they depended on the L-ascorbic acid flow rate. Notably, the surface area measurements show the same trend: the higher the flow rate, the higher the specific surface areas. The crystallites size presented an opposite trend concerning the reagent flow rate. It is coherent with the literature (Kim et al., 2007; Stichert and Schüth, 1998). The larger the crystallites size, the lower the roughness, thus the lower the surface area.

The XPS survey spectra of the Cu_2O samples show the presence of Cu, O, and C, as reported in Fig. 6a. The high-resolution spectra comprise: C1s as a reference, O1s, Cu2p, Cu LMM, and Cu valence band region. The C1s peaks have the shape of adventitious carbon due to superficial contamination. It is formed by various short-chain hydrocarbon species with single and doubly oxygen functionality (Miller et al., 2002). These peaks are present in all the samples and always have the same shape, so they are used to shift each spectrum to have the C1s peak at 284.8 eV. The peak of $Cu2p_{3/2}$ shows different shapes depending on the oxidation state of Cu. The metallic Cu^0 and the Cu^{1+} have only one peak with a smaller FWHM (full width at half maximum) than the Cu^{2+} peak at 933 eV. The Cu^{2+} has the main peak at slightly higher binding energy (933.5 eV), with a wider FWHM, and shows a satellite peak at higher energies (943 eV) with a specific shape depending on the percentage of Cu^{2+} and the formed compound. The $Cu2p_{3/2}$ peaks were mathematically deconvoluted to obtain the [Cu(0) + Cu(I)]/Cu(II) ratio as reported in previous literature (Biesinger, 2017). The peak binding energies of $Cu2p_{3/2}$ and CuLMM (Cu Auger peak) were collected and used to calculate the Modified Auger Parameter, which is correlated with the average oxidation state of sample surface (Biesinger et al., 2010). Cu^0 and Cu^{1+} were also discriminated by looking at the valence band peak shapes, which change from the oxidation state of 0 to + 1 (Fernandez et al., 2020). The evaluation of the main oxidation state obtained from all these methods were compared and they all confirm that copper is mainly present as Cu^{1+}. The valence band region at lower binding energies and the baseline were linearly fitted and their interception was calculated and used as the minimum distance of the valence band from the Fermi

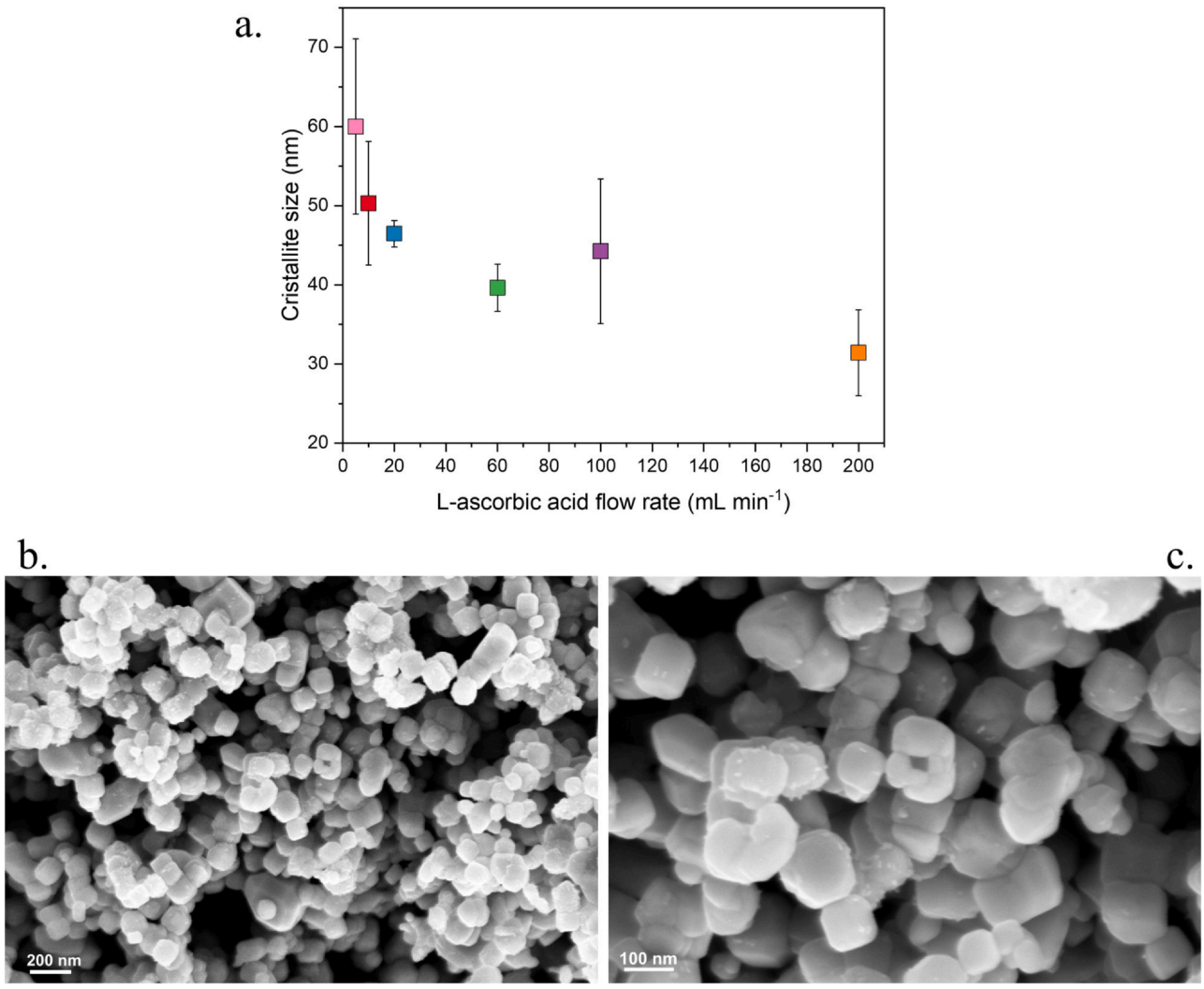


Fig. 4 – a. X-Ray Diffraction analysis, average crystallite size value for each synthesis conditions group versus the L-ascorbic acid flow rate, b. FESEM image of Cu_2O_200 with a magnification of 100 kx, c. FESEM image of Cu_2O_200 with a magnification of 250 kx.

level. All the spectra show two linear regions at low binding energies (see Section S5 and Fig. S6 in the SI). The first one, at higher energy, is more relevant and clearly visible. The second one is smaller and is located at lower energy. This behaviour is explained in literature (Feng et al., 2016) with a density of state (DOS) with a parabolic valence band with a small internal-gap state. The values of energy band gap were obtained from optical analyses, as explained previously. By knowing the distance of the valence band from the Fermi level and the energy band gap, it is possible to derivate the density of the state diagram of the copper oxide samples (see Fig. 6b. and Table S1 in SI). Notably, the L-ascorbic acid flow rate also influenced the valence band maximum position (VBM), and consequently, the conduction band minimum (CBM), which is most probably related to the crystallite sizes modification and could have a role on the photocatalysts performance. Notably, the conductivity changes from p-type semiconductor for Cu_2O_20 (in which the Fermi level is nearest to the valence band than to the conduction band) to an n-type in Cu_2O_60 and Cu_2O_100 (for which the Fermi level is nearest to the conduction band than to the valence band). In literature the conductivity type of Cu_2O results to be dependent of the pH of the precursors solutions: acidic conditions lead to n-type Cu_2O, while alkaline ones lead to p-type one (Hossain et al., 2017). In this study the synthesis is performed in alkaline environment (the pH was monitored as exposed in chapter 2.2 Cu_2O Synthesis). It is noticeable that the XPS volume analysis is confined to the surface, so it is not explanatory of the whole sample. Likewise, in the stability evaluation is Section S8 of SI, it is clearly visible that the analysis volume of XPS is confined to the surface and in that case the detected phase was not the same achieved from XRD analyses. Future work should be done to investigate deeper the energy band structure of these samples.

3.2. *Photo-electrocatalytic performance*

3.2.1. *Photo-activity of Cu_2O catalysts*

A series of tests were conducted to assess the photoelectrochemical water and CO_2 reduction capabilities of the synthesized catalysts. The tests were carried out in the setup described in Section 2.5, by soaking the photoelectrode in a 0.1 M $KHCO_3$ aqueous solution, employing a solar simulator equipped with a Xe lamp as the light source. Regarding the CV performed on the CO_2-saturated electrolyte, the potential scan was done between 0 and – 1.5 V vs. Ag/AgCl with a scan rate of 30 mV s^{-1} under simulated sunlight (AM 1.5 G spectra) at an intensity of 100 mW cm^{-2} (1 Sun). It is worth noting that the Cu_2O_200 catalyst appears to be more active because its photo-electrochemical activity (the maximum absolute

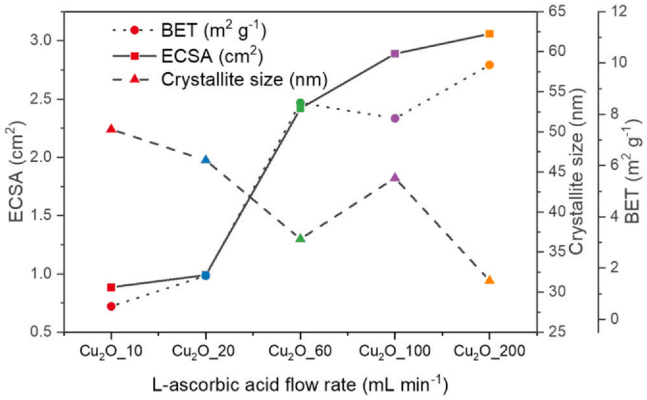


Fig. 5 – Comparison between the BET surface area, the electrochemical surface area (ECSA) and the crystallite size.

Table 1 – Values of each sample in terms of energy band gap free UV–vis spectroscopy, Cu and O atomic percentages from EDX, specific surface area from BET analysis.

Sample	E_G (eV)	Cu at%	O at%	BET (m^2 g^{-1})
Cu_2O_10	2.49 ± 0.05	68.62	31.38	-
Cu_2O_20	2.47 ± 0.04	81.77	18.23	1.71 ± 0.11
Cu_2O_60	2.51 ± 0.06	64.19	35.81	8.45 ± 0.52
Cu_2O_100	2.48 ± 0.06	59.38	40.60	7.84 ± 0.51
Cu_2O_200	2.48 ± 0.05	53.79	46.21	9.92 ± 0.46

photo-current density) is higher (–6 mA cm^{-2} at the potential of –1.5 V vs. Ag/AgCl) than that of the other materials. In fact, the crystallites size of the catalysts appears to correlate with their activity, as shown in Fig. 7. The crystal domains within the catalyst material can significantly influence its photo-electrochemical properties, such as enhancing the photo-catalytic activity and facilitating charge transfer processes. Smaller crystallite size often corresponds to a lower degree of structural order and increased surface area. Therefore, the maximum photo-current density during the CV of the Cu_2O_200 catalyst could be attributed to its smaller crystallite size. Conversely, a catalyst with bigger crystallites may have a reduced active surface area and limited charge transfer capability, leading to a lower maximum photo-current density. This study of the relationship between crystallite size and maximum photo-current density aimed to gain valuable insights into the structure-performance relationship of catalysts, aiding in the design and optimization of catalyst materials for various (photo)-electrochemical applications. Based on the observed relationship depicted in Fig. 7, it was deemed pertinent to focus the discussion on this section solely on the PEC results of Cu_2O_200. Consequently, the performance of samples with lower flow rates (Cu_2O_20 and Cu_2O_100) were also tested to explore the variations in catalyst properties. The results for these samples are reported in the Section S6, Fig. S7 and Section S8 in the SI.

Before the PEC CO_2 reduction test, a blank CV was performed with N_2-purged electrolyte to evaluate the performance of the catalyst in the working solution only towards the HER. Then, the curve was compared to that obtained in the CO_2-saturated electrolyte. The curves are reported in Fig. 8a, where the dashed line is referred to the test conducted in N_2-saturated environment, while the straight line indicates the test registered in a CO_2-saturated solution. The final total current density (accounting for the dark and light induced currents and indicating the total activity of the electrode) under CO_2 flow and illumination was almost threefold that under N_2 flow at – 1.5 V vs. Ag/AgCl. It seems to correlate with the role of the metal oxide in enhancing CO_2 adsorption and conversion with respect to the HER. The PEC activity of the Cu_2O_200 photocathode was determined through CV under illumination and dark in CO_2-saturated electrolyte solution. The total activity of the system increased by approximately 20% (from 5 to 6 mA cm^{-2}) under light conditions, demonstrating the Cu_2O role as a photo-electrocatalyst, as shown in Fig. 8b. These results agree with the behaviour observed by Guo et al. (2019). They tested Cu_2O-based photo-electrocatalysts in different saturation environments and both dark and light conditions. Their study found that under dark and N_2-saturated conditions, the electrode exhibited negligible current output. However, a significant enhancement in photo-electrochemical current was observed under illumination, with a peak increment of over 50% compared to the dark condition.

The linear polarization curves confirm the capability of the prepared materials to activate the PEC CO_2 reduction reaction toward specific products, as shown in Fig. 8c. The tests were conducted by scanning the potential from 0 to –1.5 V vs. Ag/AgCl, before in N_2-saturated conditions (dashed line) and after in CO_2 (solid line). It is once again evident that the (photo)-electrochemical activity of the catalyst was greater in the presence of CO_2 compared to the test conducted in N_2 atmosphere. The analysis performed in N_2 atmosphere demonstrated no photocurrent gain with the Cu_2O-based photo-electrocatalyst. In contrast, the results evidenced a distinct oscillatory trend due to the clear alternation between light and dark conditions in the presence of CO_2. That further evidences the role of Cu_2O as photo-electrocatalyst for the CO_2 reduction reaction. Furthermore, the onset potential of the HER was –1.3 V vs. Ag/AgCl (from the curve recorded in N_2) and approximately –0.7 V vs. Ag/AgCl for the CO_2 electroreduction reaction (from the curve recorded in CO_2) at –0.5 mA cm^{-2}. Additionally, a significant peak was observed at –0.8 V vs. Ag/AgCl under CO_2-saturated electrolyte condition. That cathodic branch could be attributed to the reduction of intermediates adsorbed on the catalyst surface and to the reduction of Cu^{1+} to Cu^0. Furthermore, a CA as performed at –1.2 V vs. Ag/AgCl (equal to around –0.6 V vs. RHE) for 10 min. Fig. 8d shows the current density trend. The test was conducted under CO_2 saturation conditions, alternating light and dark conditions every 1 min. The photocurrent gain generated by the catalyst during illumination conditions was of about 0.055 mA cm^{-2}. Moreover, the result remained consistent throughout the

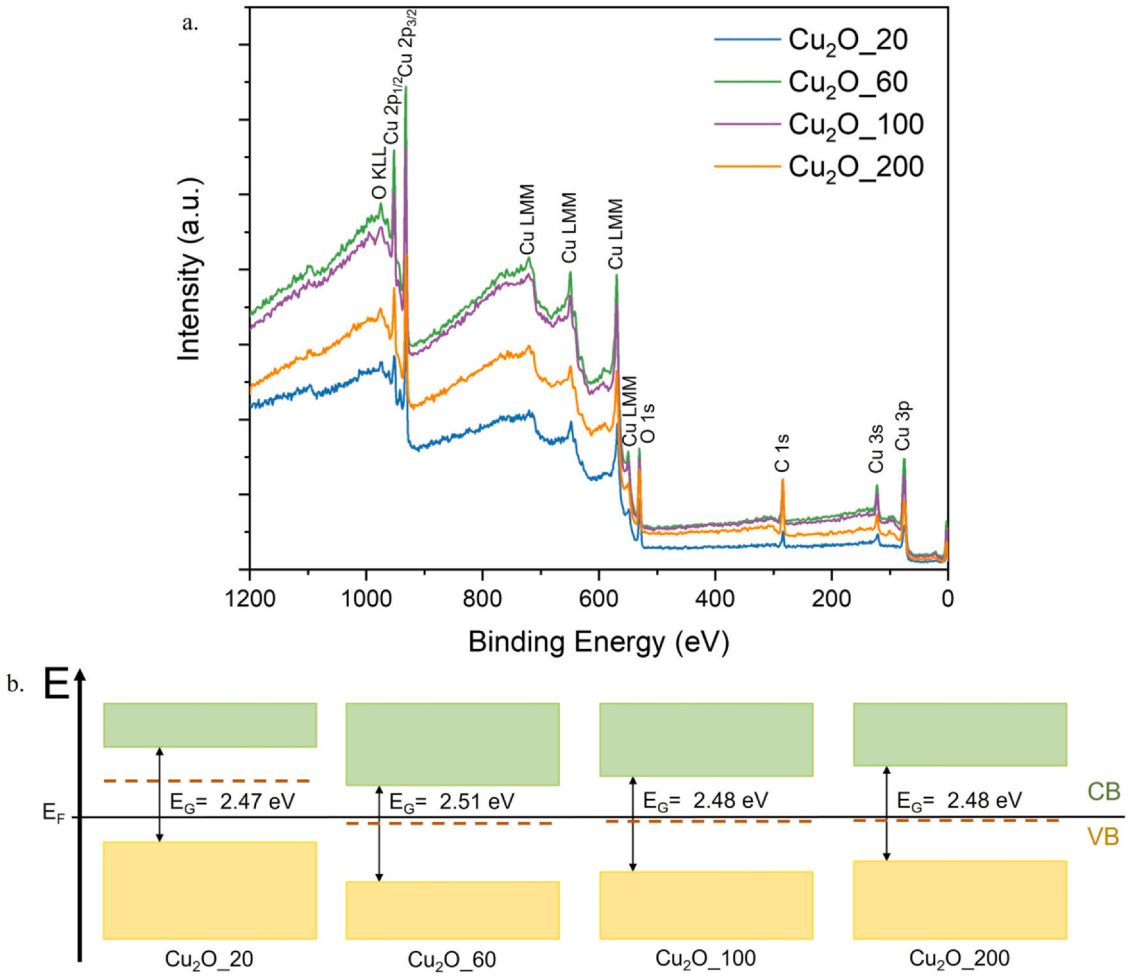


Fig. 6 – XPS analyses. a. Survey spectra of the samples Cu_2O_20, Cu_2O_60, Cu_2O_100 and Cu_2O_200 with highlighted the peaks relatable to Cu, O, and C. b. energy band diagram of the copper oxide samples: energy band gap obtained from the UV–vis spectroscopy analyses, energy band levels retrieved from XPS valence band spectra. The dotted line represents the internal-gap level.

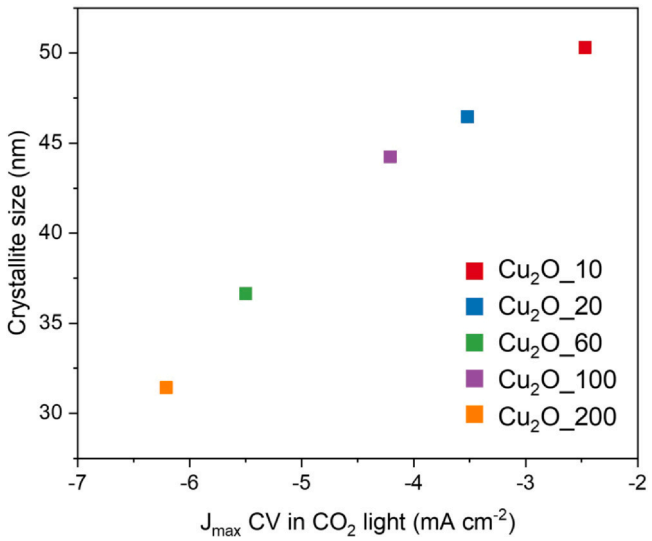


Fig. 7 – Trend of the relationship between maximum current density detected during CV in CO_2 (range: 0. –1.5 V vs. Ag/AgCl) under solar simulated enlightenment and crystallite size for the 5 different Cu_2O samples.

experiment, highlighting the good stability of the catalyst under such operative conditions. By comparing the CA result with a similar material deposited onto a Cu foam, studied by Zhang et al.(Zhang et al., 2023) substantial differences can be noticed. In the described study, conducted under a bias voltage of 0 V versus RHE with 0.2 mol L^{-1} Na_2SO_4 as the electrolyte solution, the Cu_2O/CF photocathode exhibited a rapid decay of the photocurrent density within the initial 300 s, followed by a slower decay trend. Notably, in this study, the Cu_2O does not show a decay trend after 300 s

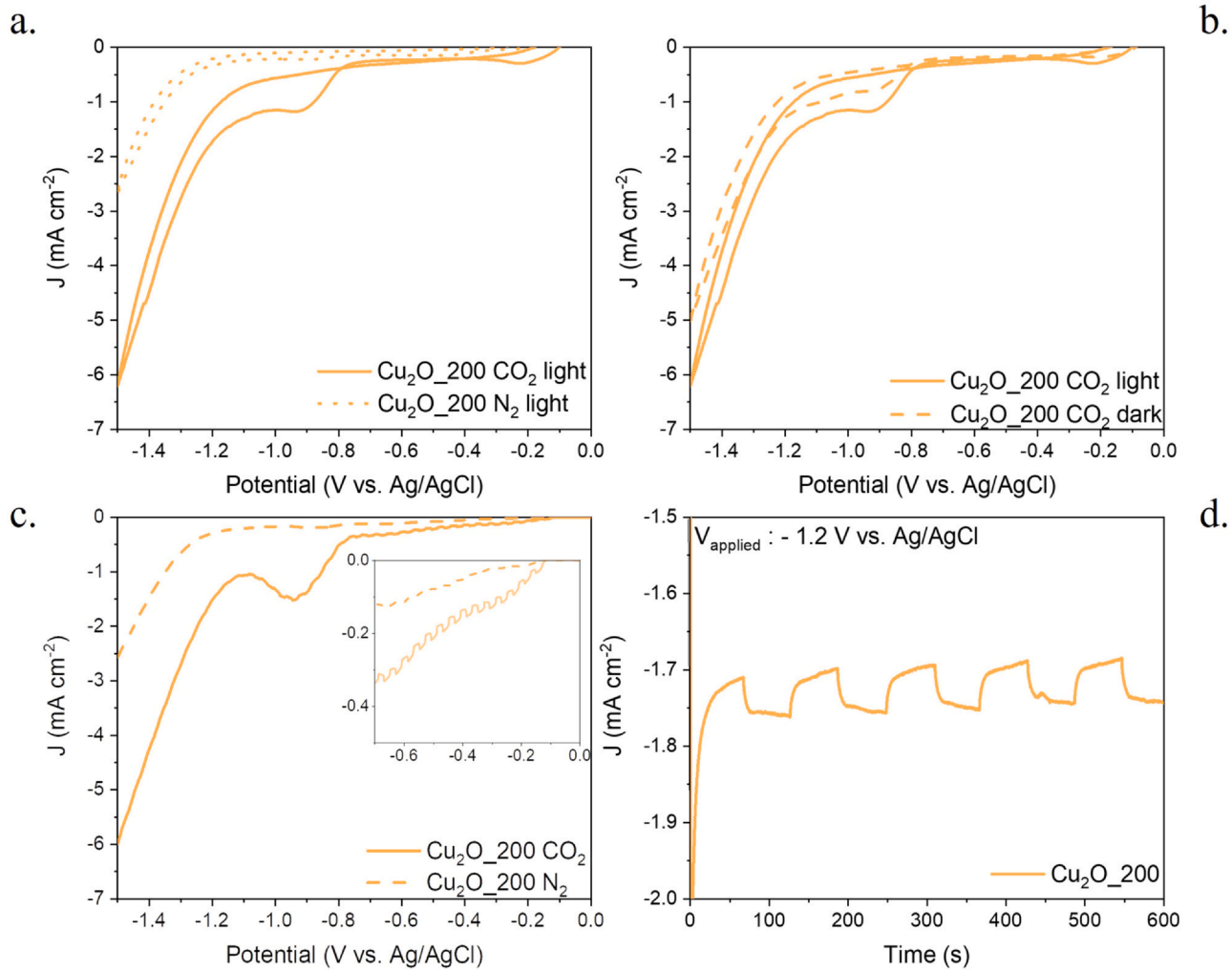


Fig. 8 – Results of PEC tests of Cu_2O_200 sample, in particular: (a) comparison of CVs carried out in N_2 and CO_2 saturated environment under illumination, (b) comparison of CVs carried out in CO_2 saturated environment both in dark and light conditions, (c) LSVs tests carried out in in N_2 and CO_2 saturated environment, with chopped illumination (each 2 s), and (d) chronoamperometry test 10 min lasting with an applied potential of –1.2 V vs. Ag/AgCl, under chopped light each 1 min.

during the CAs. This suggests that the experimental conditions or catalyst preparation applied in the two works may have differed, leading to variations in the photocurrent stability and decay behaviour.

Electrochemical Impedance Spectroscopy (EIS) was employed to further characterize the photo-electrochemical behaviour of the different synthesised materials. The Nyquist plots obtained are composed of two different time constants (τ); the equivalent circuit chosen for the interpretation of the data and the fitting is depicted in Fig. 9a. The circuit comprises two elements: the resistance R and the constant phase element (CPE); the CPE is used to model non-ideal capacitors and is very useful when modelling data obtained from the non-ideal system. The electrochemical system was represented as follows: R_1 models the resistance of the electrolyte solution and, as expected, it is the same for all the materials tested and does not change under illumination conditions or in the presence of CO_2 (see Section S7 and Fig. S10 in the SI); the parallel composed by R_2 and CPE_1 models the resistance and the capacitance that the charges undergo inside the material of the electrode itself; R_3 represents the resistance for the electron transfer between the surface of the electrode and the species adsorbed onto it; R_3 is the main parameter that will be discussed herein because it models the ease with which the electrons are transferred to a CO_2 molecule to be reduced; this is confirmed since it is the only potential-dependent resistance of the model (Fig. 9b). CPE_2 represents the electrochemical double layer formed between the electrolyte and the surface of the electrode.

All the data discussed in this section were obtained by performing EIS at the onset potential measured via CV at –1.1 V vs. Ag/AgCl (3 M NaCl). In this way, it is possible to compare the different samples in conditions where the faradaic current starts to become non-negligible without being disturbed by the vigorous formation of bubbles on the surface of the electrode due to the evolution of gaseous products such as CO and H_2. In a typical experiment, an AC sinusoidal voltage (amplitude A = 0.010 mV) was superimposed to the experiment's DC voltage, and the system's response was recorded at the frequencies between 10^6 and 0.01 Hz.

As it is visible from Fig. 9a, when CO_2 is dissolved into the electrolyte, the resistance R3 is lower than in N_2, indicating the higher activity of the Cu_2O catalyst towards the electron transfer to the CO_2 molecules adsorbed onto the electrode surface; the lower resistance in a CO_2-saturated atmosphere at the onset shows the preference of the electrode to transfer the supplied electrons to CO_2 instead of water at the electrode surface. Furthermore, in a CO_2-saturated atmosphere, the illumination of the system showed an additional decrease in the R_3 value, also

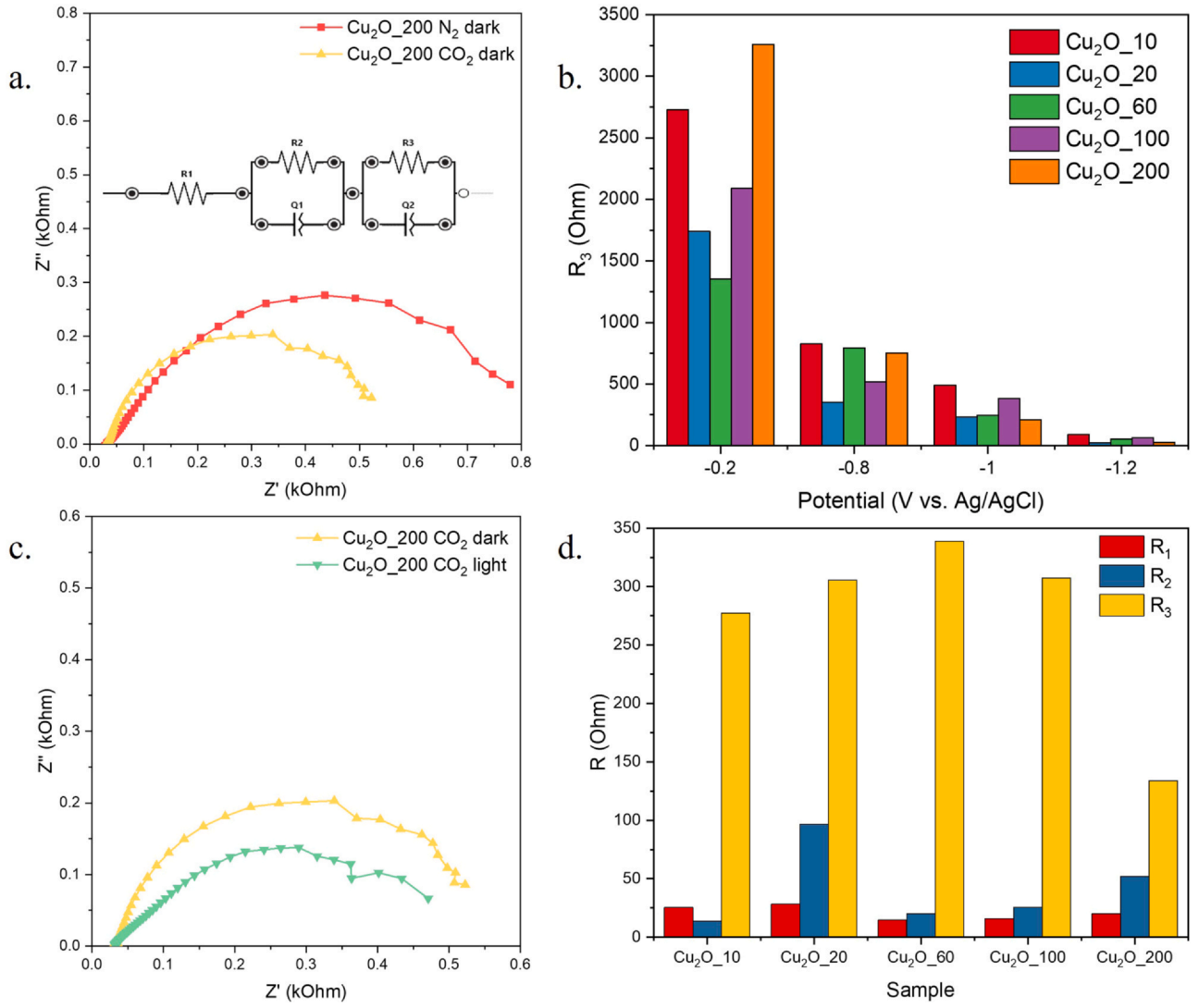


Fig. 9 – EIS measurements: a. Nyquist plot of Cu_2O_200 in N_2 and CO_2 saturated environment in dark conditions and equivalent circuit, b. Nyquist plot of Cu_2O_200 in CO_2 saturated environment in dark and light conditions, c. fitted values of the resistances (R_1, R_2, and R_3) at –1.1 V vs. Ag/AgCl for all the samples, d. fitted values for R_3 evaluated at different potentials (–0.2, –0.8, –1.0, and –1.2 V vs. Ag/AgCl) for all the samples.

indicating the photoactivity of the material under examination (Fig. 9c). These considerations agree with the photo-electrochemical data previously discussed.

From a comparison of the fittings obtained by the test of different samples in the CO_2-saturated atmosphere and under illumination conditions, Cu_2O_200 displays the lower R3 value when compared with the other materials synthesized, indicating the best photo-electrocatalytic activity at the onset potential (Fig. 9d).

3.2.2. *Selectivity of Cu_2O catalysts*

Fig. 10a shows the selectivity towards C-based products of the Cu_2O_200 catalyst (the most photoactive one) in comparison with such of the Cu_2O_20 and Cu_2O_100 materials, which were tested under the same conditions to investigate an eventual correlation between the crystallites size and the catalysts selectivity. The tests were carried out at a constant current density of –3 mA cm^{-2}. The overtime potential profile is quite stable, without any significant current changes at the applied current density, indicating stability of the catalyst. However, the potential drops of around 10% after 120 min of PEC CO_2 reduction, stabilizing at –1.5 V vs. Ag/AgCl for Cu_2O_200 (see Fig. 10 b). During the whole development of the test, the gaseous compounds were detected via μ-GC, while liquid samples were collected after the test and injected into the HPLC for the analysis. The obtained products were H_2, CO and Formate. In the three cases, most of the consumed electrons were exploited for the HER, reaching a selectivity to H_2 between 76.8% and 81.5%. Such result could be attributed to the aqueous based electrolyte and the low CO_2 solubility causing mass transport limitations of the reagent to the catalyst surface in the H-cell used for the tests. The total selectivity towards C-compounds was of approximately 28–23%, divided into CO and Formate. The Cu_2O_100 sample shows the best selectivity towards C-products, with a percentage of 23.2%, although it generally showed a similar performance to the Cu_2O_200. For all the photo-cathodes, the total FE remained low (around 55%, see Fig. S9 in SI). The difference with respect to 100% was probably related to the catalyst restructuration. Indeed, as reported in the Section S8 of the SI, chopped CA (under light and dark conditions) demonstrated that the Cu_2O_100 electrode decreased its photoactivity over time because Cu_2O suffers of reduction to Cu^0

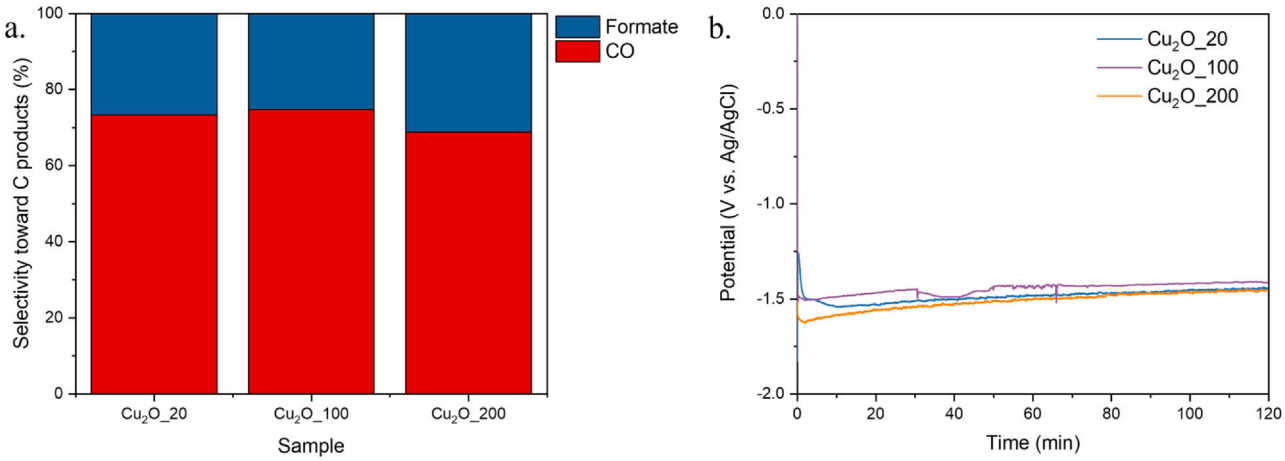


Fig. 10 – Results of PEC CP test of Cu_2O_20, Cu_2O_100, and Cu_2O_200 samples carried out for 2 h at –3 mA cm^{-2}. a: selectivity towards C-based products, b: detected potential during the CP.

during the operation (as confirmed by XRD analyses of the electrode before and after the CA test (see Fig. S13). This can be attribute to electron injection in the valence band after holes photogeneration (Chang et al., 2016). This effect can also be the reason of the potential decrease (in absolute value) during the CP, since metallic Cu is more conductive than the Cu_2O semiconductor material.

In a previous work of some of us (Zoli et al., 2023b), a Cu_2O/SnO_2 composite was synthetised by co-precipitation method with the aim to protect the Cu^{1+} oxidation state. In such work, the presence of ethanol was detected (Faradaic Efficiency of around 9%), and the selectivity was predominantly directed towards formate due to the inclusion of tin. In the case of the here described Cu_2O nanocubes, only the C_1 compounds formation was observed, with a main selectivity towards H_2 and CO gaseous products. It is hypothesized that the catalyst structural characteristics may have influenced selectivity, along with potential modifications occurring during the testing protocol. Further PEC studies, coupled with comprehensive product analysis, can provide valuable insights into understanding and guiding the catalyst selectivity. Additionally, exploring the implementation of protective shell for the Cu_2O nanocubes could offer an intriguing approach to stabilize the Cu^{1+} oxidation state, while tailoring and altering the catalyst's selectivity. Alternatively, as demonstrated in a recent work by Miró Serra and co-workers (Miró et al., 2023), shifting to a different class of electrolytes like ionic liquids (in their specific case, they used BMIM·TfO) may yield significantly higher proportions of C_2 compounds. On the other hand, Zhang et al.(Zhang et al., 2019) synthesized a Cu_2O core covered with a SnO_2 protective shell and obtained higher FEs towards CO concerning bare Cu_2O.

3.2.3. *Core-shell Cu_2O/SnO_2*

Following the synthesis method reported in this work, a sample of Cu_2O_ 100 (the most selective sample towards C-products) was covered with an overlayer of tin oxide. Further details about the synthetic method, firstly developed by Zhang et al., (Zhang et al., 2019) and then adapted by Zoli and coworkers (Zoli et al., 2023a) are reported in Section S9 in SI. Such catalyst was called $Cu_2O_SnO_2$. The plot of the gaseous products evolution during a 2-hour lasting chronopotentiometry test, together with further details on the PEC test, are reported in Section S9 in SI. Notably, this sample showed a much higher selectivity towards C-based products than the pristine Cu_2O catalysts, with a CO/H_2 ratio of about 2:1, and an excellent stability throughout the entire 120-minute test. A nearly constant production of H_2 of around 200 ppm was observed, while the CO remained constant between 400 and 500 ppm during the full test. Starting from these good results, the duration of the test was further increased to evaluate a longer-term stability. A 5-hour test was done, and the gas products results are reported in Fig. 11a. In this case, in addition to the confirmed stability in CO production throughout the whole test duration, the CO

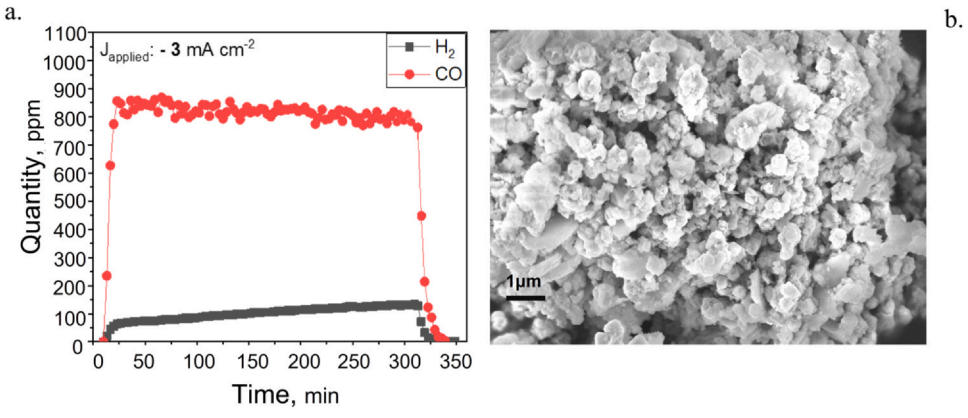


Fig. 11 – (a) Gaseous products evolution during chronopotentiometry test on Cu_2O_100_SnO_2 at $J_{applied}$ = –3 mA cm^{-2} for 5 h, (b) insights on the Sn presence into the catalyst, in particular: FESEM image.

concentration remained constant at an average value of about 800 ppm throughout the test duration. H_2 never exceeded 150 ppm and remained stable during the test. Finally, the CO:H_2 ratio was calculated to be approximately 7, while the pristine Cu_2O_100 catalysts (without any protective layer) showed a CO:H_2 ratio of around 1:3. Hence, by adding the SnO_2 protective layer, as noticed from the insights reported in Fig. 11b, the C-based molecules production increased and maintained a good stability throughout the whole duration of the test. The percentages of each element of interest were obtained from EDX analysis and the Cu:Sn ratio is around 3.3.

The potential during the test was attested around –1.65 V vs. Ag/AgCl. Considering this notable result, further investigation of this material and the SnO_2 deposition procedure should be performed.

4. Conclusions

In this paper, Cu_2O nanocubes synthesis was optimized by controlling the flow rate of addition of the different reagents: $CuCl_2$ (Cu precursor), NaOH (precipitation agent) and L-ascorbic acid (reducing agent). Moreover, the effect of the L-ascorbic acid flow rate on the physico-chemical and optical properties of the photo-catalysts was investigated through different characterization techniques (XRD, FESEM, EDX, UV-Vis spectroscopy, XPS, BET, ECSA). Some relevant characteristics of the catalyst were not affected like the Cu_2O crystalline phase, the cubic nanostructure of the particles and the energy band gap, while different replicas prepared under the same synthesis conditions demonstrated an excellent reproducibility of the process. Instead, the crystallites size, specific surface area and electrochemical surface area strongly depended on the reducing agent flow rate. The higher was the flow rate of addition of L-ascorbic acid, the lower the crystallites size and the higher the surface area and ECSA, which in turns leads to a higher photo-electrochemical activity. The photo-current density at the same potential is higher (in absolute value) for the samples synthesized with higher flow rates. This study demonstrates how important is the control of the synthesis condition in terms of repeatability and tunability of the photo-catalytic properties. Starting from this, a broad spectrum of synthesis conditions could be investigated to obtain a broader range of tuneable characteristics, including the co-precipitation or the preparation of core-shell structures, while ensuring the synthesis scalability. Herein, a notable result was also reported by recovering the Cu_2O with a shell of SnO_2, which demonstrated to be an efficient approach to avoid the Cu^{+1} reduction and guarantee the photocatalyst stability over time. Thus, such Cu_2O/SnO_2 synthesis could be further tuned to reach relevant photo-current densities coupled with a high stability for a prospective application of the scaled-up photocatalysts for different environmental and energy applications (Guzmán et al., 2022; Raudaskoski et al., 2009; Toyir et al., 2001; Zoli et al., 2023b).

Declaration of Competing Interest

The authors declare that they have no known competing financial interests or personal relationships that could have appeared to influence the work reported in this paper.

Acknowledgements

The research leading to these results has received funding from the European Union's Horizon 2020 Research and Innovation Action program under the SunCoChem project (Grant Agreement No 862192). The authors thank Federico Dattila (https://orcid.org/0000-0001-8195-3951) for FESEM and EDX analysis and Camilla Galletti for the support in the analysis of XRD measurements.

Appendix A. Supporting information

Supplementary data associated with this article can be found in the online version at doi:10.1016/j.cherd.2023.09.047.

References

Ahmad, T., Liu, S., Sajid, M., Li, K., Ali, M., Liu, L., Chen, W., 2022. Electrochemical CO_2 reduction to C_{2+} products using Cu-based electrocatalysts: a review. Nano Res. Energy 1, e9120021. https://doi.org/10.26599/NRE.2022.9120021

Biesbroek, Robbert, Bowen, Kathryn, Lawrence, Judy, Pörtner, H.-O., Roberts, D.C., AdamsI, H., Adelekan, Adler, C., Adrian, R., Aldunce, P., Ali, E., Begum, R.A., Bednar-Friedl, B., Kerr, R.B., Biesbroek, R., Birkmann, J., Bowen, K., Caretta, M.A., Carnicer, J., Castellanos, E., Cheong, T.S., Chow, W., Cissé, G., Clayton, S., Constable, A., Cooley, S., Costello, M.J., Craig, M., Cramer, W., Dawson, R., Dodman, D., Efitre, J., Garschagen, M., Gilmore, E.A., Glavovic, B., Gutzler, D., Haasnoot, M., Harper, S., Hasegawa, T., Hayward, B., Hicke, J.A., Hirabayashi, Y., Huang, C., Kalaba, K., Kiessling, W., Kitoh, A., Lasco, R., Lawrence, J., Lemos, M.F., Lempert, R., Lennard, C., Ley, D., Lissner, T., Liu, Q., Liwenga, E., Lluch-Cota, S., Löschke, S., Lucatello, S., Luo, Y., Mackey, B., Mintenbeck, K., Mirzabaev, A., Möller, V., Vale, M.M., Morecroft, M.D., Mortsch, L., Mukherji, A., Mustonen, T., Mycoo, M., Nalau, J., New, M., Africa, A.O.South, Ometto, J.P., O'Neill, B., Pandey, R., Parmesan, C., Pelling, M., Pinho, P.F., Pinnegar, J., Poloczanska, E.S., Prakash, A., Preston, B., Racault, M.-F., Reckien, D., Revi, A., Rose, S.K., Schipper, E.L.F., Schmidt, D.N., Schoeman, D., Shaw, R., Simpson, N.P., Singh, C., Solecki, W., Stringer, L., Totin, E., Trisos, C.H., Trisurat, Y., van Aalst, M., Viner, D., Wairu, M., Warren, R., Wester, P., Wrathall, D., Ibrahim, Z.Z., 2022. 2022: Technical Summary. Climate Change 2022: Impacts, Adaptation, and Vulnerability. Contrib. Work. Group II Sixth Assess. Rep. Intergov. Panel Clim. Change. https://doi.org/10.1017/9781009325844.002

Biesinger, M.C., 2017. Advanced analysis of copper X-ray photoelectron spectra. Surf. Interface Anal. 49, 1325–1334. https://doi.org/10.1002/SIA.6239

Biesinger, M.C., Lau, L.W.M., Gerson, A.R., Smart, R.S.C., 2010. Resolving surface chemical states in XPS analysis of first row transition metals, oxides and hydroxides: Sc, Ti, V, Cu and Zn. Appl. Surf. Sci. 257, 887–898. https://doi.org/10.1016/J.APSUSC.2010.07.086

Blunden, J., Arndt, D.S., 2020. State of the climate in 2019. Bull. Am. Meteor. Soc. 101, S1–S8. https://doi.org/10.1175/2020BAMSSTATEOFTHECLIMATE_INTRO.1

Chang, X., Wang, T., Zhang, P., Wei, Y., Zhao, J., Gong, J., 2016. Stable aqueous photoelectrochemical CO_2 reduction by a Cu_2O dark cathode with improved selectivity for carbonaceous products. Angew. Chem. Int. Ed. 55, 8840–8845. https://doi.org/10.1002/ANIE.201602973

Chiu, Y.H., Lai, T.H., Kuo, M.Y., Hsieh, P.Y., Hsu, Y.J., 2019. Photoelectrochemical cells for solar hydrogen production: challenges and opportunities. APL Mater. 7, 80901. https://doi.org/10.1063/1.5109785/123144

Das, S., Pérez-Ramírez, J., Gong, J., Dewangan, N., Hidajat, K., Gates, B.C., Kawi, S., 2020. Core–shell structured catalysts for thermocatalytic, photocatalytic, and electrocatalytic

conversion of CO_2. Chem. Soc. Rev. 49, 2937–3004. https://doi.org/10.1039/C9CS00713J

Fang, M.J., Tsao, C.W., Hsu, Y.J., 2020. Semiconductor nanoheterostructures for photoconversion applications. J. Phys. D. Appl. Phys. 53. https://doi.org/10.1088/1361-6463/AB5F25

Feng, N., Liu, F., Huang, M., Zheng, A., Wang, Q., Chen, T., Cao, G., Xu, J., Fan, J., Deng, F., 2016. Unravelling the efficient photocatalytic activity of boron-induced Ti_{3+} species in the surface layer of TiO_2. Sci. Rep. 2016 6:1 6, 1–9. https://doi.org/10.1038/srep34765

Feng, Y., Lin, S., Huang, S., Shrestha, S., Conibeer, G., 2015. Can Tauc plot extrapolation be used for direct-band-gap semiconductor nanocrystals? J. Appl. Phys. 117. https://doi.org/10.1063/1.4916090

Fernandez, V., Kiani, D., Fairley, N., Felpin, F.X., Baltrusaitis, J., 2020. Curve fitting complex X-ray photoelectron spectra of graphite-supported copper nanoparticles using informed line shapes. Appl. Surf. Sci. 505, 143841. https://doi.org/10.1016/J.APSUSC.2019.143841

Guo, L., Cao, J., Zhang, J., Hao, Y., Bi, K., 2019. Photoelectrochemical CO_2 reduction by Cu_2O/Cu_2S hybrid catalyst immobilized in TiO_2 nanocavity arrays. J. Mater. Sci. 54, 10379–10388. https://doi.org/10.1007/S10853-019-03615-4/FIGURES/5

Guzmán, H., Salomone, F., Bensaid, S., Castellino, M., Russo, N., Hernández, S., 2022. CO_2 conversion to alcohols over Cu/ZnO catalysts: prospective synergies between electrocatalytic and thermocatalytic routes. ACS Appl. Mater. Interfaces 14, 517–530. https://doi.org/10.1021/ACSAMI.1C15871/ASSET/IMAGES/MEDIUM/AM1C15871_M003.GIF

Handoko, A.D., Tang, J., 2013. Controllable proton and CO_2 photoreduction over Cu_2O with various morphologies. Int J. Hydrog. Energy 38, 13017–13022. https://doi.org/10.1016/J.IJHYDENE.2013.03.128

Haryński, Ł., Olejnik, A., Grochowska, K., Siuzdak, K., 2022. A facile method for Tauc exponent and corresponding electronic transitions determination in semiconductors directly from UV–Vis spectroscopy data. Opt. Mater. (Amst.) 127. https://doi.org/10.1016/j.optmat.2022.112205

Hossain, M.A., Al-Gaashani, R., Hamoudi, H., Al Marri, M.J., Hussein, I.A., Belaidi, A., Merzougui, B.A., Alharbi, F.H., Tabet, N., 2017. Controlled growth of Cu2O thin films by electrodeposition approach. Mater. Sci. Semicond. Process 63, 203–211. https://doi.org/10.1016/j.mssp.2017.02.012

Hsieh, P.-Y., Wu, J.-Y., Chang, T.-F.M., Chen, C.-Y., Sone, M., Hsu, Y.-J., 2020. Near infrared-driven photoelectrochemical water splitting: Review and future prospects. https://doi.org/10.1016/j.arabjc.2020.05.025.

Huang, W.C., Lyu, L.M., Yang, Y.C., Huang, M.H., 2012. Synthesis of Cu_2O nanocrystals from cubic to rhombic dodecahedral structures and their comparative photocatalytic activity. J. Am. Chem. Soc. 134, 1261–1267. https://doi.org/10.1021/JA209662V/SUPPL_FILE/JA209662V_SI_001.PDF

Jubu, P.R., Yam, F.K., Igba, V.M., Beh, K.P., 2020. Tauc-plot scale and extrapolation effect on bandgap estimation from UV–vis–NIR data – A case study of β-Ga_2O_3. J. Solid State Chem. 290, 121576. https://doi.org/10.1016/J.JSSC.2020.121576

Kim, D.S., Han, S.J., Kwak, S.Y., 2007. Synthesis and photocatalytic activity of mesoporous TiO_2 with the surface area, crystallite size, and pore size. J. Colloid Interface Sci. 316, 85–91. https://doi.org/10.1016/J.JCIS.2007.07.037

Miller, D.J., Biesinger, M.C., McIntyre, N.S., 2002. Interactions of CO_2 and CO at fractional atmosphere pressures with iron and iron oxide surfaces: one possible mechanism for surface contamination. Surf. Interface Anal. 33, 299–305. https://doi.org/10.1002/SIA.1188

Miró, R., Guzmán, H., Godard, C., Gual, A., Zammillo, F., Schubert, T.J.S., Iliev, B., Chiodoni, A., Hernández, S., de los Bernardos, M.D., 2023. Solar-driven CO_2 reduction catalysed by hybrid supramolecular photocathodes and enhanced by ionic liquids. Catal. Sci. Technol. 13, 1708–1717. https://doi.org/10.1039/D2CY01523D

Osterloh, F.E., 2008. Inorganic materials as catalysts for photochemical splitting of water. Chem. Mater. 20, 35–54. https://doi.org/10.1021/CM7024203/ASSET/IMAGES/LARGE/CM-2007-024203_0005.JPEG

Qin, G., Zhang, Y., Ke, X., Tong, X., Sun, Z., Liang, M., Xue, S., 2013. Photocatalytic reduction of carbon dioxide to formic acid, formaldehyde, and methanol using dye-sensitized TiO_2 film. Appl. Catal. B 129, 599–605. https://doi.org/10.1016/J.APCATB.2012.10.012

Raudaskoski, R., Turpeinen, E., Lenkkeri, R., Pongrácz, E., Keiski, R.L., 2009. Catalytic activation of CO_2: Use of secondary $CO_2$for the production of synthesis gas and for methanol synthesis over copper-based zirconia-containing catalysts. Catal. Today 144, 318–323. https://doi.org/10.1016/J.CATTOD.2008.11.026

Report of the Conference of the Parties on its twenty-sixth session, held in Glasgow from 31 October to 13 November 2021, 2032.

Sahoo, G.S., Tripathy, S.P., Joshi, D.S., Kulkarni, M.S., 2020. Development of an algorithm for precise and automated determination of optical band gap from Tauc analysis: case studies using alpha-irradiated CR-39 detectors. Radiat. Eff. Defects Solids 175, 1127–1139. https://doi.org/10.1080/10420150.2020.1810039

Semiconductor nanocrystals possessing broadly size- and facet-dependent optical properties | Enhanced Reader [WWW Document], n.d. URL (accessed 9.19.22).

Shukla, P.R., Skea, J., Reisinger, A., Slade, R., Fradera, R., Pathak, M., Al, A., Malek, K., Diemen, B.R. van, Hasija, A., Lisboa, G., Luz, S., Malley, J., Mccollum, D., Some, S., 2022. Climate Change 2022 Mitigation of Climate Change Working Group III Contribution to the Sixth Assessment Report of the Intergovernmental Panel on Climate Change Summary for Policymakers Edited by.

Stichert, W., Schüth, F., 1998. Influence of crystallite size on the properties of zirconia. Chem. Mater. 10, 2020–2026. https://doi.org/10.1021/CM980705O/ASSET/IMAGES/LARGE/CM980705OH00001.JPEG

Sun, S., Zhang, Xiaojing, Yang, Q., Liang, S., Zhang, Xiaozhe, Yang, Z., 2018. Cuprous oxide (Cu_2O) crystals with tailored architectures: a comprehensive review on synthesis, fundamental properties, functional modifications and applications. Prog. Mater. Sci. 96, 111–173. https://doi.org/10.1016/J.PMATSCI.2018.03.006

Toyir, J., De la Piscina, P.R., Fierro, J.L.G., Homs, N., 2001. Catalytic performance for CO_2 conversion to methanol of gallium-promoted copper-based catalysts: influence of metallic precursors. Appl. Catal. B 34, 255–266. https://doi.org/10.1016/S0926-3373(01)00203-X

Tsao, C.W., Fang, M.J., Hsu, Y.J., 2021. Modulation of interfacial charge dynamics of semiconductor heterostructures for advanced photocatalytic applications. Coord. Chem. Rev. 438, 213876. https://doi.org/10.1016/J.CCR.2021.213876

Unfccc, n.d. ADOPTION OF THE PARIS AGREEMENT - Paris Agreement text English.

Wang, Y., He, D., Chen, H., Wang, D., 2019. Catalysts in electro-, photo- and photoelectrocatalytic CO_2 reduction reactions. J. Photochem. Photobiol. C: Photochem. Rev. 40, 117–149. https://doi.org/10.1016/J.JPHOTOCHEMREV.2019.02.002

Woldu, A.R., Huang, Z., Zhao, P., Hu, L., Astruc, D., 2022. Electrochemical CO_2 reduction (CO_2RR) to multi-carbon products over copper-based catalysts. Coord. Chem. Rev. 454, 214340. https://doi.org/10.1016/J.CCR.2021.214340

Xie, H., Wang, T., Liang, J., Li, Q., Sun, S., 2018. Cu-based nanocatalysts for electrochemical reduction of CO_2. Nano Today 21, 41–54. https://doi.org/10.1016/J.NANTOD.2018.05.001

Zhang, S.N., Li, M., Hua, B., Duan, N., Ding, S., Bergens, S., Shankar, K., Luo, J.L., 2019. A rational design of Cu_2O–SnO_2 core-shell catalyst for highly selective CO_2-to-CO conversion. ChemCatChem 11, 4147–4153. https://doi.org/10.1002/CCTC.201900395

Zhang, W., Bai, Y., Tian, M., Liu, Y.G., Hou, J., Li, C., Jiang, H.Y., Tang, J., 2023. Improvement of the photoelectrochemical stability of Cu_2O photocathode by Ph-C≡C-Cu grafting.

Adv. Mater. Interfaces 10. https://doi.org/10.1002/admi.202201380

Zoli, M., Guzmán, H., Sacco, A., Russo, N., Hernández, S., 2023a. Cu_2O / SnO_2 heterostructures: role of the synthesis procedure on PEC CO_2 Conversion. Materials 16, 4497. https://doi.org/10.3390/ma16134497

Zoli, M., Roldán, D., Guzmán, H., Castellino, M., Chiodoni, A., Bejtka, K., Russo, N., Hernández, S., 2023b. Facile and scalable synthesis of Cu_2O-SnO_2 catalyst for the photoelectrochemical CO_2 conversion. Catal. Today 413–415, 113985. https://doi.org/10.1016/J.CATTOD.2022.12.016